Original research article

Adsorption Science & Technology
Volume 44: 1–23
© The Author(s) 2026
Article reuse guidelines:
sagepub.com/journals-permissions
DOI: 10.1177/02636174261418492
journals.sagepub.com/home/adt
Sage

Enhanced fixed-bed column adsorption using a ternary MgO-impregnated eggshell–kaolin composite: Toward an efficient and sustainable fluoride removal technology

Aisha Murgen Kitemangu[1,2], Revocatus Lazaro Machunda[1], Mwemezi Johaiven Rwiza[1], Nyemaga Masanje Malima[2], Andrew Toyi Banyikwa[2] and Gordian Rocky Mataba[1]

Abstract

In this study, a ternary MgO-impregnated eggshell–kaolin (EKM) composite was synthesized and evaluated for fluoride removal from water under fixed-bed column adsorption. The composite, prepared by co-precipitation and wet impregnation, was characterized using XRD, FTIR, SEM–EDX, and Brunauer–Emmet–Teller analyses. Results confirmed successful integration of the three components, yielding a mesoporous structure with a surface area of 158.5 $m^2\ g^{-1}$. The composite exhibited good defluoridation performance under varying operational conditions. Higher bed depth and lower flow rate enhanced adsorption capacity, achieving up to 6.35 $mg\ g^{-1}$ at 10 $mg\ L^{-1}$ influent fluoride concentration. Breakthrough data were well described by the Thomas, Clark, and Yoon–Nelson models ($R^2 \geq 0.94$) at lower influent concentration, moderate flow rate, and greater bed depth, while the bed depth service time model confirmed a linear increase in service time with bed depth. The adsorbent maintained good regeneration ability across four cycles. Co-existing anions showed interference with the uptake of F^-, with inhibitory effects following the order: $PO_4^{3-} > SO_4^{2-} > NO_3^- > Cl^-$. The study estimated that 11.11 g of EKM composite yields 2 L of safe water for less than USD1. These results highlight the EKM composite as an efficient and sustainable adsorbent for practical defluoridation applications.

---

[1] School of Materials, Energy, Water and Environmental Sciences (MEWES), The Nelson Mandela African Institution of Science and Technology (NM-AIST), Arusha, Tanzania
[2] Department of Chemistry, College of Natural and Mathematical Sciences, The University of Dodoma, Dodoma, Tanzania

Corresponding author:
Aisha Murgen Kitemangu, School of Materials, Energy, Water and Environmental Sciences (MEWES), The Nelson Mandela African Institution of Science and Technology (NM-AIST), P.O. Box 447, Arusha, Tanzania; Department of Chemistry, College of Natural and Mathematical Sciences, The University of Dodoma, P.O. Box 338, Dodoma, Tanzania.
Emails: aishak@nm-aist.ac.tz; aisha.kitemangu@udom.ac.tz

Keywords
fixed-bed column adsorption, breakthrough curve, composite, adsorption capacity, defluoridation

Received: October 15, 2025; accepted: January 8, 2026

Introduction

Securing access to safe and clean\ water is one of the most pressing challenges facing the world today (Okafor et al., 2024). Among the various threats to water quality, fluoride contamination in groundwater is particularly concerning, especially in arid and semi-arid regions where groundwater often serves as the primary source of drinking water (Kimambo et al., 2019). Elevated fluoride levels, commonly of geogenic origin, exceed the World Health Organization (WHO) recommended the limit of $1.5\,\mathrm{mg\,L^{-1}}$, leading to widespread health disorders, including dental and skeletal fluorosis (Owusu-Agyeman et al., 2019; Solanki et al., 2021). These health impacts disproportionately affect rural and low-income communities, further compounding issues of inequality and access to safe water. Africa bears a disproportionate burden, with over 40 million individuals affected, particularly in East African countries like Kenya, Ethiopia, and Tanzania (Ijumulana et al., 2021; Workeneh et al., 2019). Similarly, in parts of Asia, including India and China, approximately 90 million people are affected by fluorosis (Chen et al., 2010). Fluoride contamination not only endangers public health but also undermines the broader goal of water sustainability, making it a critical barrier to achieving Sustainable Development Goal 6, which aims to ensure the availability and sustainable management of water and sanitation for all (Tortajada, 2020). Addressing this challenge requires the development of affordable, efficient, and locally accessible defluoridation technologies that can improve water quality without imposing financial or technical burdens on resource-limited communities.

Many technologies have been applied to meet the enforceable drinking water standard for fluoride, including nano-filtration (Owusu-Agyeman et al., 2019), coagulation (Solanki et al., 2021), chemical precipitation (Wang et al., 2021), electrodialysis (Wang et al., 2019), electrochemical oxidation (Lin et al., 2021), ion exchange (Feng et al., 2021), reverse osmosis (Lin et al., 2021), and adsorption (Nabbou et al., 2019). Among these techniques, adsorption has been widely applied and accepted due to its inexpensiveness, low sludge production, ease of operation, regeneration capability, and high fluoride removal efficiency (Chaudhary et al., 2021; Fadaei, 2021; Lee et al., 2021). Conventional adsorbents and composites such as graphene oxide composites (Prathibha et al., 2020), activated alumina (Alhassan et al., 2021), metal–organic frameworks (Tang et al., 2022), hydroxyapatite (Rathnayake et al., 2022), MgO nano-particles (Borgohain et al., 2020), eggshells (Lee et al., 2021), kaolin (Ayalew, 2020), and bone char (Nigri et al., 2020), have been developed and applied for water defluoridation. However, many of these materials are limited by potential secondary contamination, effectiveness only under acidic conditions, low performance, limited accessibility, and unsuitability for large-scale application (Das et al., 2021; Wan et al., 2021). In this regard, there is a pressing need for alternative materials that are locally available, effective, and environmentally friendly.

As an alternative, waste eggshells have been widely studied as low-cost, natural adsorbents for fluoride removal due to their high calcium content, primarily in the form of calcium carbonate (Lee et al., 2021). However, their practical application in water defluoridation is limited by factors such as low adsorption capacity, narrow pH effectiveness, slow kinetics, structural instability, and poor reusability (Assami and Messaitfa, 2023; Lee et al., 2021). To address these limitations, an eggshell–kaolin composite was synthesized at varying ratios for defluoridation investigations (Senarathna et al., 2024). The composite with a 50:50 ratio demonstrated the highest fluoride removal efficiency of 53% (Senarathna et al., 2024). Despite exhibiting a higher adsorption capacity than eggshells alone, the overall capacity of the composite remained comparatively low (0.08 mg g^{-1}). Impregnating an eggshell–kaolin composite with a metal oxide possessing a high affinity for fluoride ions may offer a promising strategy for enhanced defluoridation.

MgO exhibits a high affinity for F^- ions due to its high concentration of reactive surface ions (Lewis acids), high ionic character, high porosity, large surface area, and the presence of lattice-bound and isolated hydroxyl groups, thereby enhancing adsorption efficiency across a wide pH range (Borgohain et al., 2020). Kaolin clay, on the other hand, provides structural stability, increases surface area, and improves mechanical strength (Ayalew, 2020; Borgohain et al., 2020; Setiadji et al., 2018). Meanwhile, eggshell-derived calcium serves as a natural and abundant source of active sites (Assami and Messaitfa, 2023).

To date, no studies have incorporated magnesium oxide (MgO) into an eggshell–kaolin framework. Given the strong affinity of MgO for fluoride, high surface reactivity, and stability over a wide pH range, its integration into a biogenic mineral composite could potentially enhance adsorption efficiency, rate, and reusability. However, the adsorption behavior, mechanistic pathways, and practical performance of such a composite remain unexplored.

Moreover, several studies have investigated the defluoridation of water through batch adsorption experiments, with a primary focus on the synthesis and characterization of adsorbents, as well as isotherm, kinetic, and thermodynamic studies. While these investigations are essential for assessing the effectiveness of various adsorbents under controlled conditions, the findings from batch adsorption cannot accurately represent the dynamic behavior of adsorption processes, nor can they be reliably extrapolated to large-scale or field applications. To address this limitation, the present study employed fixed-bed column adsorption for the removal of fluoride ions (F^-) using an MgO-impregnated eggshell–kaolin (EKM) composite adsorbent.

Building on recent advancements in the application of natural and metal oxide-based adsorbents for water treatment, this study presents the synthesis, characterization, and evaluation of EKM composite material for the removal of fluoride from drinking water. The composite was prepared by integrating eggshell, kaolin, and MgO, thereby harnessing the calcium-rich composition of eggshells, the structural stability of kaolin clay, and the strong affinity of MgO for fluoride ions. The defluoridation performance of the composite was investigated under fixed-bed column adsorption conditions. Specifically, the effects of flow rate, initial fluoride concentration, and background electrolytes on the adsorption capacity were examined. Breakthrough curve analyses were further conducted using the Thomas, Clark, Yoon–Nelson, and bed depth service time (BDST) models to elucidate the adsorption mechanisms and column kinetics. In addition, the reusability of the composite was assessed through multiple adsorption–desorption cycles to evaluate its potential for practical application.

Materials and methods

Materials

This study used waste eggshells collected from Cafe la Zain restaurant in Arusha and kaolin obtained from Malangali, Iringa. The chemicals or reagents employed include $Mg(NO_3)_2$, NaOH, HCl, and NaF. All chemicals used were of analytical grade and sourced from Thermo Fisher Scientific. Additionally, deionized water was used for washing, rinsing, and preparing solutions.

Preparation of EKM composite

Eggshells and kaolin clay were placed in laboratory basins, thoroughly washed, and rinsed with deionized water to remove any adhering impurities. Both eggshells and kaolin were allowed to settle in water for 1 h, then decanted, and oven-dried at 105 °C for 24 h to remove moisture. The drying process was followed by grinding using a heavy-duty blender, and the powder was then sieved through 250 μm sieves. The materials were packed in plastic bags and stored for further analysis.

Co-precipitation and wet impregnation methods were used to prepare the ternary EKM composite (Setiadji et al., 2018; Suwattanamala et al., 2017). Exactly 500 mL of 0.2 M $Mg(NO_3)_2$ was placed in a 1000 mL beaker on a hot plate magnetic stirrer (cat. no. CB162, Sr. no. R300001128, 230 V, 50 Hz, 550 W, 15 A) equipped with a suspended pH meter and a thermometer. A temperature of 80 °C was set to speed up the reaction under constant stirring. Then, 1 M NaOH was added to the solution dropwise until a pH of 9 was reached, and the precipitate of $Mg(OH)_2$ began to form. A 50:50 ratio of eggshell and kaolin was weighed separately and added to a beaker containing $Mg(OH)_2$, after which the mixture was stirred on a hot plate magnetic stirrer overnight. The mixture was filtered using a suction filtration pump, and the final product was dried overnight in an oven at 105 °C. The resulting product was calcined in a furnace for 3 h at 900 °C. The synthesis yielded ∼4 g of MgO, corresponding to an Mg/MgO mass ratio of 1:1.66. Upon incorporation into 60 g of eggshell–kaolin support prepared at a 50:50 (w/w) ratio, the resulting composite exhibited an MgO loading of 6.3 wt%.

Physico-chemical characterization of EKM composite

The Quanta Chrome NOVA 1200e surface area and porosity analyzer was used to evaluate the surface area and porosity characteristics of the EKM composite using the Brunauer–Emmet–Teller (BET) method. Under the BET method, vapors were extracted from all samples using a 0.1 mTorr pressure and vacuum at 573 K for 6 h. Measurements were made by physical adsorption using pure liquid nitrogen at 77.35 K. Scanning electron microscopy coupled with an energy dispersive X-ray spectrometer (SEM–EDX), Oxford Instruments, X-Max, Ultra55, and Zeiss, was used to perform the morphological analysis and to study the elemental composition of the EKM composite before and after adsorption. A Fourier-transform infrared (FTIR) (Bruker Optics ALPHA-E) spectrometer was used to elucidate the functional groups present on EKM before and after adsorption. The samples were prepared by first oven-drying for 2 h, cooled in a desiccator, and ground to a fine consistency in an agate mortar to ensure homogeneity. Approximately 10 mg of the sample was evenly spread on an Attenuated Total Reflectance crystal, and the pressure arm was applied to achieve a good contact between the sample and the crystal surface. Background spectra were collected prior to each measurement, and the sample spectra were acquired in the range of 4000–400 cm^{-1} at 4 cm^{-1} resolution with 32 co-added scans. The crystallographic properties of EKM were determined using an X-ray diffractometer (Rebaku SmartLab XRD) with an analyzer scanning mode, employing a CuKα wavelength (λ) of 1.54 Å, at 40 kV, and 30 mA, with a step size of 0.02 Å and a scanning speed of 0.2 Å s^{-1}.

Preparation of stock solution

Sodium fluoride (NaF) was used as a fluoride source to prepare a stock solution of fluoride. Exactly, 0.2 g of NaF was dissolved in 2 L of deionized water to prepare a 100 mg L^{-1} stock solution, followed by serial dilution to obtain working solutions of different fluoride concentrations (5, 10, and 20 mg L^{-1}).

Estimation of fluoride ion

Fluoride concentrations in water samples were determined using an ion-selective electrode (HACH, HQ 30d Flexi, Intellical™ Fluoride, ISEF121, SN: 162362938003) following the manufacturer's instructions. The electrode was calibrated with fluoride standard solutions of

0.1, 0.5, 1.0, 5.0, and 10.0 mg L^{-1} prepared in total ionic strength adjustment buffer (TISAB). Water samples were mixed with an equal volume of TISAB to maintain a constant ionic strength and pH, and the electrode was immersed until stable readings were obtained. Fluoride concentrations were calculated from the calibration curve, and each sample was analyzed in triplicate to ensure accuracy and reproducibility.

Fixed-bed column adsorption

Fixed-bed column adsorption experiments were carried out using a cylindrical glass column with an internal diameter and column height of 1.04 and 40 cm, respectively. A glass wool (~2 cm) was placed at the bottom of the column to prevent loss of the adsorbent from the column and promote uniform distribution of the influent solution through the cross-section of the column. The bulk density determined from the dry adsorbent packed in the column and the volume of the packed bed was 0.59 g cm^{-3}, while the particle density and bed porosity were 2.69 g cm^{-3} and 0.78, respectively. The column was packed with a wetted EKM adsorbent, and the system was operated under gravity flow, with the influent supplied from an elevated reservoir. The experiment was conducted at varying flow rates (1, 1.5, and 2 mL min^{-1}), initial fluoride concentrations (5, 10, and 20 mg L^{-1}), and bed depths (2, 4, and 6 cm). The flow rate was adjusted using controllable faucets and was performed at an initial fluoride concentration of 5 mg L^{-1} and a bed depth of 2 cm. The effect of initial fluoride concentration was studied at a flow rate of 1 mL min^{-1} and a bed depth of 2 cm. The bed depth was varied at a fixed initial fluoride concentration of 5 mg L^{-1} and a flow rate of 1 mL min^{-1}. The effluent samples were collected at 60-min intervals and analyzed for fluoride concentration. The experiment continued until the concentration at the outlet of the column almost equaled the concentration at the inlet. Breakthrough curves were plotted for the evaluation of the fixed-bed column adsorption.

Breakthrough curve analysis

The performance of the fixed-bed column adsorption was evaluated through breakthrough curve analysis, where the ratio of effluent to influent concentration (C_t / C_0) was plotted as a function of time (t). The breakthrough time (t_b) was defined as the time to break through the curve penetration point, while the exhaustion time (t_e) referred to the point at which the effluent concentration approached 99% of the influent concentration. These parameters provide practical indicators of the column's operational lifespan under the tested conditions. The breakthrough time and exhaustion time, along with the bed depth (Z), were used to evaluate the mass transfer zone (MTZ) using equation (1). The MTZ is the length of the fixed-bed column adsorption zone that represents the efficiency of the adsorbent used.

$$\mathrm{MTZ}\ \ (\mathrm{cm}) = Z\left(1 - \frac{t_b}{t_e}\right) \tag{1}$$

The empty bed contact time (EBCT), representing the average residence time of the solution within the column, was calculated using the below equation:

$$\mathrm{EBCT} = \frac{V}{Q} = \frac{A \times Z}{Q} \tag{2}$$

where V (cm^3) is the column bed volume, A (cm^2) is the cross-sectional area of the column, Z (cm) is the bed depth, and Q (mL min^{-1}) is the influent flow rate.

The total amount of fluoride ions retained on the column bed at a given concentration (q_{tot}) and influent flow rate (Q) was calculated using the below equation:

$$q_{tot} = \frac{Q \times A}{1000} = \frac{Q \times C_0}{1000} \int_{t=0}^{t=\mathrm{total}} \left(1 - \frac{C_t}{C_0}\right) dt \tag{3}$$

where Q (mL min^{-1}) and A represent the influent flow rate and the area under the breakthrough curve, respectively.

The volume of effluent that can be treated by the column was calculated from the influent flow rate and exhaustion time using the below equation:

$$V_{\mathrm{eff}} = Q \times t_{\mathrm{e}} \tag{4}$$

The bulk density, ρ_{b} (g cm^{-3}), which defines the mass of the dry adsorbent, M_{d} (g), per unit volume of the packed bed, V_{t} (cm^3) was determined using the below equation:

$$\rho_{\mathrm{b}} = \frac{M_{\mathrm{d}}}{V_{\mathrm{t}}} \tag{5}$$

The volume of the packed bed (V_t) is inclusive of the volume of the adsorbent and the void volume (V_{v}) (the pore space between the adsorbent particles). The void volume can be determined from the weight of saturated adsorbent, W_{s} (g), weight of dry adsorbent, W_{d} (g), and the density of water, ρ_{w} (g cm^{-3}), as shown below:

$$V_{\mathrm{v}} = \frac{W_{\mathrm{s}} - W_{\mathrm{d}}}{\rho_{\mathrm{w}}} \tag{6}$$

The particle density, ρ_{p} (g cm^{-3}) of the adsorbent and the bed porosity, ε_{b}, can be found using the below equations, respectively:

$$\rho_{\mathrm{b}} = \frac{M_{\mathrm{d}}}{V_{\mathrm{t}} - V_{\mathrm{v}}} \tag{7}$$

$$\varepsilon_{\mathrm{b}} = 1 - \frac{\rho_{\mathrm{b}}}{\rho_{\mathrm{p}}} \tag{8}$$

Results and discussion

Physico-chemical characterization of the adsorbent

XRD analysis. Figure 1 shows the XRD patterns of eggshells, kaolin, MgO, and the ternary EKM composite. The eggshell diffraction peaks appear at $2\theta = 15.98°$, 17.8°, 23.08°, 26.15°, 29.45°, 30.82°, 32.50°, 34.15°, 39.28°, 42.21°, 45.50°, 47.22°, 48.60°, 50.84°, 54.30°, 62.59°, and 64.20°. The peaks at 29.45°, 32.50°, 34.15°, 47.22°, 50.84°, and 54.30° indicate that $CaCO_3$ in the eggshells decomposed to CaO during thermal activation at 900 °C (Ayodeji et al., 2018; Senarathna et al., 2024). The kaolin diffraction peaks appear at $2\theta = 15.80°$, 17.47°, 19.49°, 20.80°, 22.19°, 23.86°, 26.44°, 35.49°, 36.69°, 39.28°, 45.02°, 50.10°, 54.83°, 60.00°, and 68.00°. The broad hump observed between 15° and 30° could be attributed to the amorphous metakaolin phase resulting from the thermal treatment (Ayodeji et al., 2018; Senarathna et al., 2024). The diffraction peaks of MgO were observed at $2\theta = 17.9°$, 34.04°, 38.19°, 42.74°, 55.51°, 58.63°, 62.14°, and 78.54°. The XRD pattern of the EKM composite (Figure 1(d)) displays diffraction peaks corresponding to eggshell, kaolin, and MgO, confirming successful composite formation. The reflections observed at $2\theta = 29.45°$, 34.15°, 47.22°, 50.84°, and 54.30° are attributed to CaO, formed through the thermal decomposition of $CaCO_3$ from the eggshells (Senarathna et al., 2024). Peaks appearing at $2\theta = 20.80°$, 23.86°, 26.44°, and 68.00° are characteristic of kaolin, while those at $2\theta = 17.9°$, 34.04°, 42.74°, and 62.14° correspond to the crystalline MgO phase. The co-existence of these peaks, with slight broadening, suggests dispersion of MgO within the eggshell–kaolin matrix without forming new crystalline phases. This observation is consistent with the findings reported by Senarathna et al. (2024). The XRD results confirm structural integration and indicate that the phases remained stable after composite formation, thereby

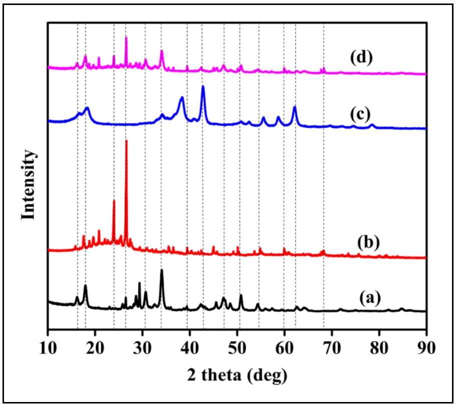

Figure 1. XRD pattern of (a) eggshell, (b) kaolin, (c) MgO, and (d) EKM composite recorded using Cu Kα radiation ($\lambda = 1.5406$ Å) at a scan rate of 2° min^{-1} in the 2θ range of 2°–90°. EKM: MgO-impregnated eggshell–kaolin.

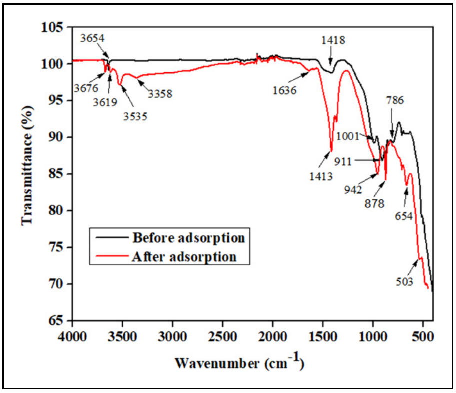

Figure 2. FTIR spectra of EKM adsorbent before and after adsorption, in the 4000–400 cm^{-1} range. EKM: MgO-impregnated eggshell–kaolin.

enhancing crystallinity and providing a heterogeneous surface that is favorable for adsorption.

FTIR analysis. Figure 2 shows the FTIR spectra of the EKM adsorbent before and after adsorption. Noticeable changes from the spectra include peak shifting, changes in peak intensity, as well as the disappearance and emergence of some peaks after adsorption. Before adsorption, the FTIR spectrum of EKM shows a sharp band at 3654 cm^{-1} corresponding to the unassociated surface hydroxyl groups (–OH), originating from both the eggshell and MgO components, which tend to adsorb moisture from the ambient air. While this peak disappeared after adsorption of F^{-}, new small, broader, and less intense peaks emerged at 3676, 3619, 3535, and 3358 cm^{-1}. These changes may be attributed to the altered surface hydroxyl groups or structural modification through ion exchange with F^{-} ions. The new peak at 1630 cm^{-1} is ascribed to surface hydroxyl groups, suggesting the strong affinity of oxides (MgO) in the adsorbent for water molecules (Liu et al., 2023). The peak at 1418 cm^{-1} shifted to a lower wavenumber at 1413 cm^{-1} while another new peak appeared at 878 cm^{-1} after adsorption of F^{-} (Chakraborty and Naskar, 2021; He et al., 2020). In the region between 1001 and 654 cm^{-1}, the main functional groups are associated with Si–O and Al–OH from kaolin in the EKM adsorbent (Ayalew, 2020; Deju et al., 2020). After adsorption, the changes observed in the region include, increase in sharpness and intensity of peaks, as well as disappearance and emergence of some peaks, which reflect the perturbations in Al–O vibrations, that are consistent with the formation of surface Al–F bonds. Importantly, a new absorption peak appeared at 503 cm^{-1}, which can be attributed to the formation of metal–fluoride bonds, most likely Mg–F. This is in line with the findings of Wang et al. (2023), who reported Mg–F stretching vibration at 503 cm^{-1}.

SEM–EDX analysis. SEM–EDX results presented in Figure 3 show the surface morphology and composition of the EKM adsorbent before and after adsorption. Before adsorption, the SEM image of EKM (Figure 3(a)) shows a heterogeneous and compact microstructure with distinguishable clusters and flaky plates. The image exhibits slight aggregation, interstices, well-distributed roughness, and surface texture, which is ideal for F^{-} ions interaction. After adsorption (Figure 3(b)), the interstices appeared diminished, and the surface showed partial coverage by deposited phases, which could be ascribed to successful fluoride uptake through surface coverage or chemical bonding. EDX spectrum of the EKM sample after adsorption (Figure 3(c)) further confirmed the capture of F^{-} ion on the composite, which is evidenced by the distinct F peak alongside Mg, Ca, Al, Si, and O.

BET analysis. The results presented in Table 1 show the BET surface area values and porosity characteristics of eggshells, kaolin, MgO, and EKM adsorbent samples. The observed BET surface area (158.5 m^{2} g^{-1}), pore radius (19.1 Å), and pore volume (0.2 cm^{3} g^{-1}) for the EKM composite are correspondingly larger than those of eggshells, kaolin, and MgO. The larger surface area and porosity characteristics of the composite suggest its porous nature, which can facilitate the uptake of F^{-} ions from the solution.

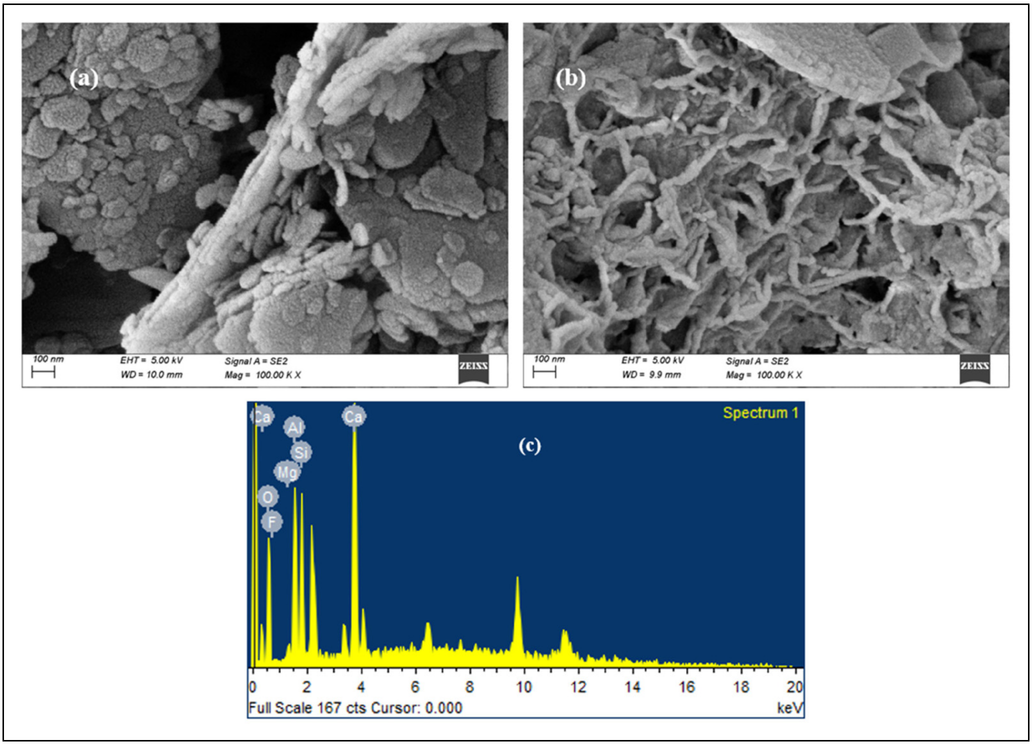

Figure 3. (a) SEM image of EKM before adsorption, (b) SEM image of EKM after adsorption, (c) EDX spectrum after adsorption (accelerating voltage = 5 kV and magnification = 100k×). EKM: MgO-impregnated eggshell–kaolin.

Table 1. BET surface area and porosity features of eggshells, kaolin, MgO, and EKM composite recorded at 77 K using the multi-point and BJH methods.

Parameter	Eggshells	Kaolin	MgO	EKM composite
Specific surface area ($m^2 g^{-1}$)	137.0	144.2	88.8	158.5
Pore radius (Å)	16.9	19.1	16.9	19.1
Total pore volume ($cm^3 g^{-1}$)	0.2	0.3	0.2	0.6

BET: Brunauer-Emmett-Teller; BJH: Barrett-Joyner-Halenda; EKM: MgO-impregnated eggshell–kaolin.

The adsorption–desorption isotherms (Figure 4) reveal distinct textural characteristics of the studied materials characterized according to the International Union of Pure and Applied Chemistry (IUPAC) classification. Figure 4(a) shows that the calcined eggshells approach type IV isotherm with negligible hysteresis. Calcined kaolin and MgO (Figure 4(b) and (c)) display type IV isotherms with pronounced H3 hysteresis loops, characteristic of mesoporous materials, indicative of non-rigid aggregates of plate-like particles that give rise to slit-shaped pores (Lin et al., 2021; Wang et al., 2020). Figure 4(d) shows that the EKM composite also follows a type IV isotherm with moderated H3 hysteresis, reflecting a hierarchical mesoporous structure arising from the

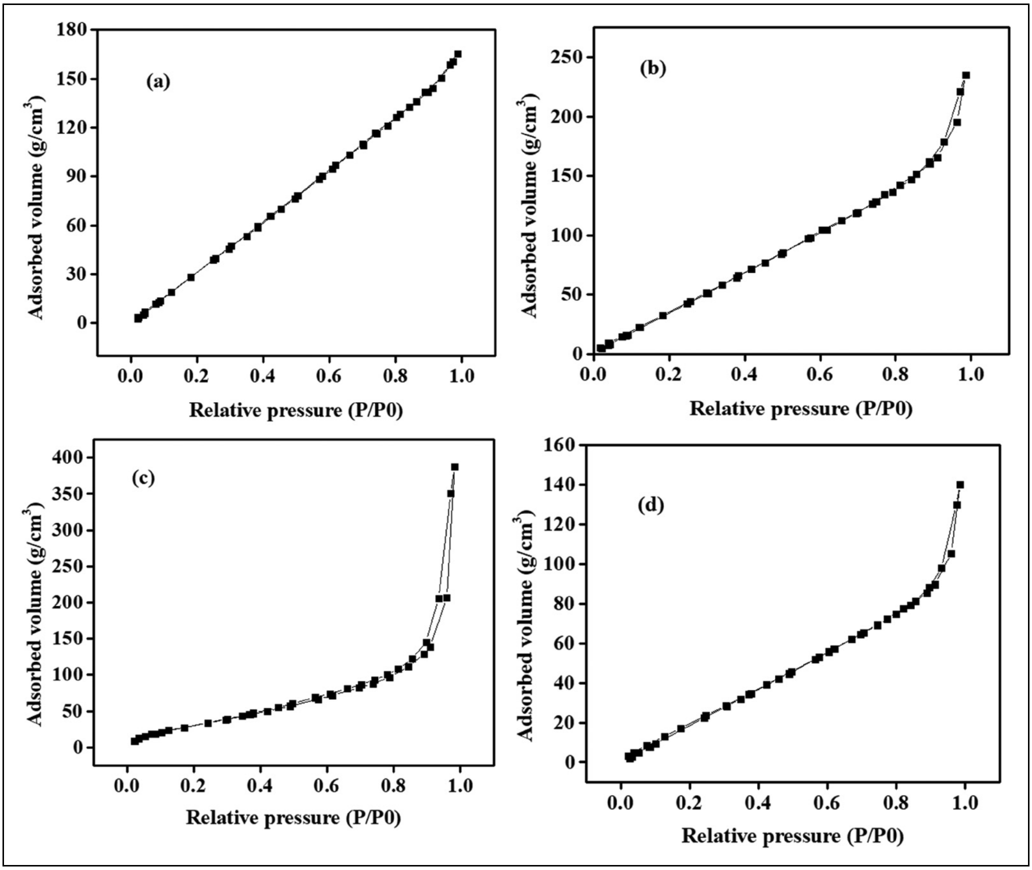

Figure 4. Adsorption–desorption curve for (a) CE, (b) CK, (c) CM, and (d) EKM recorded at 77 K using the multi-point and BJH methods. BJH: Barrett-Joyner-Halenda; EKM: MgO-impregnated eggshell–kaolin.

synergistic combination of the parent materials, which is favorable for enhanced adsorption performance. Estimation of the pore size distributions of the materials using liquid nitrogen as an adsorbate at 77 K is presented in Figure 5. Figure 5(a) to (d) shows that most pores lie in the mesoporous range of 2 nm $< d <$ 50 nm, signifying that the prepared EKM composite is potentially effective in adsorption of F^- ions from water (Lin et al., 2021). Previous studies have reported mesoporous materials of comparable pore size distribution, hysteresis loop, and isotherm indicative of non-rigid aggregates of plate-like particles that give rise to slit-shaped pores (Lin et al., 2021; Wang et al., 2020).

Fixed-bed column adsorption of fluoride onto EKM adsorbent

Effect of flow rate. Flow rate is a key parameter for evaluating the performance of a fixed-bed adsorption column. The impact of flow rate on breakthrough curves was analyzed at different flow rates (1, 1.5, and 2 mL min^{-1}). Experiments were performed with an initial fluoride concentration of 5 mg L^{-1}, a bed depth of 2 cm, at 25 °C, and pH 7. The results, shown in Figure 6(a) and Table 2, illustrate how breakthrough curves change with increasing influent flow rate and include the parameters derived from these curves. Increasing the influent flow rate through the column resulted in a decrease in

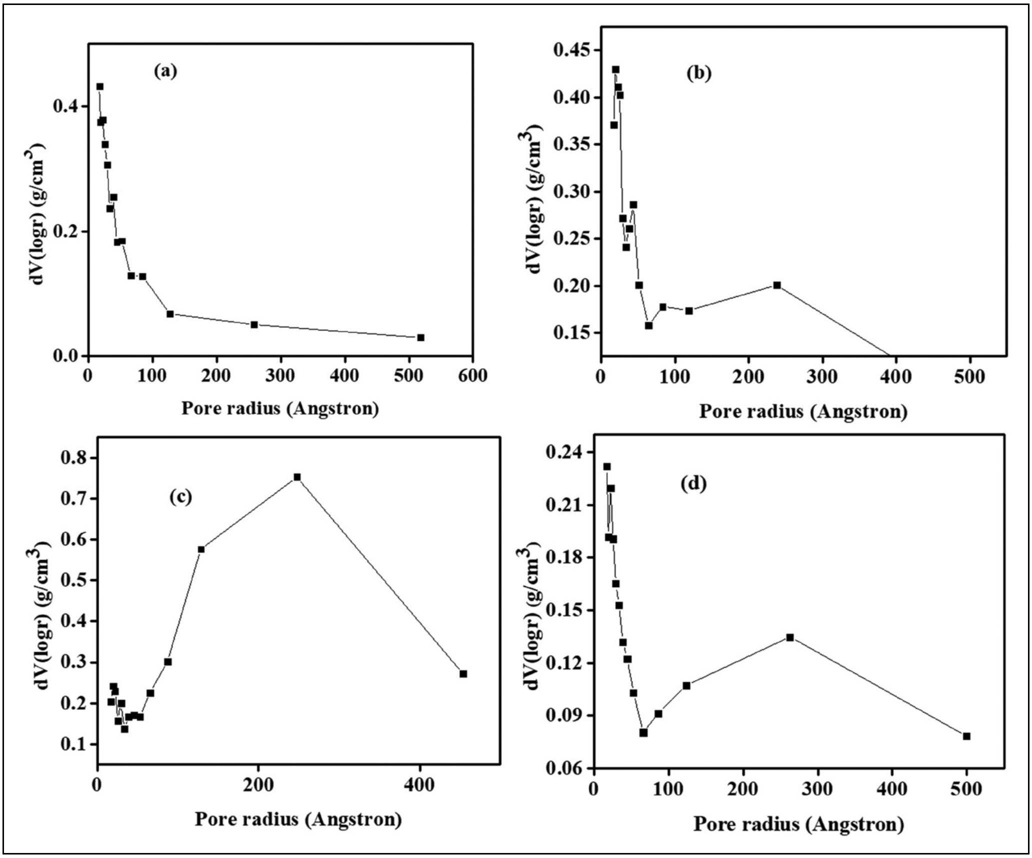

Figure 5. Pore size distribution for (a) CE, (b) CK, (c) CM, and (d) EKM recorded at 77 K using the multi-point and BJH methods. BJH: Barrett-Joyner-Halenda; EKM: MgO-impregnated eggshell–kaolin.

breakthrough times (from 300 to 180 and 120 min) and exhaustion times (from 1140 to 840 and 660 min). Consequently, the MTZ widened, while the EBCT decreased. Furthermore, higher flow rates led to a reduction in both the effluent volume (1140, 840, and 660 mL) and the equilibrium adsorption capacity (2.84, 2.51, and 1.14 mg g^{-1}). The variations may be attributed to the shorter residence time at higher flow rates, which reduces the contact time between fluoride ions in the solution and the EKM adsorbent in the column bed, causing the ions to exit the column before equilibrium is achieved. A similar phenomenon was reported to cause a decrease in the equilibrium adsorption capacity (Kumari et al., 2021; Zhang et al., 2019).

Effect of initial fluoride concentration. The effect of the initial fluoride concentration on the breakthrough curves was studied using solutions with concentrations of 5, 10, and 20 mg L^{-1}. The experiment was conducted at a bed depth of 2 cm, a flow rate of 1 mL min^{-1} at 25 °C, and pH 7. The results in Figure 6(b) and Table 2 show that the increase in the initial fluoride concentration (5, 10, and 20 mg L^{-1}) has led to the decrease of the breakthrough times (300, 180, and 60 min), the exhaustion times (1140, 900, and 720 min) and the effluent volume (1140, 900, and 720 mL). The observations could be attributed to the saturation of the available active sites of the adsorbent at higher initial fluoride concentration (Kumari et al., 2021).

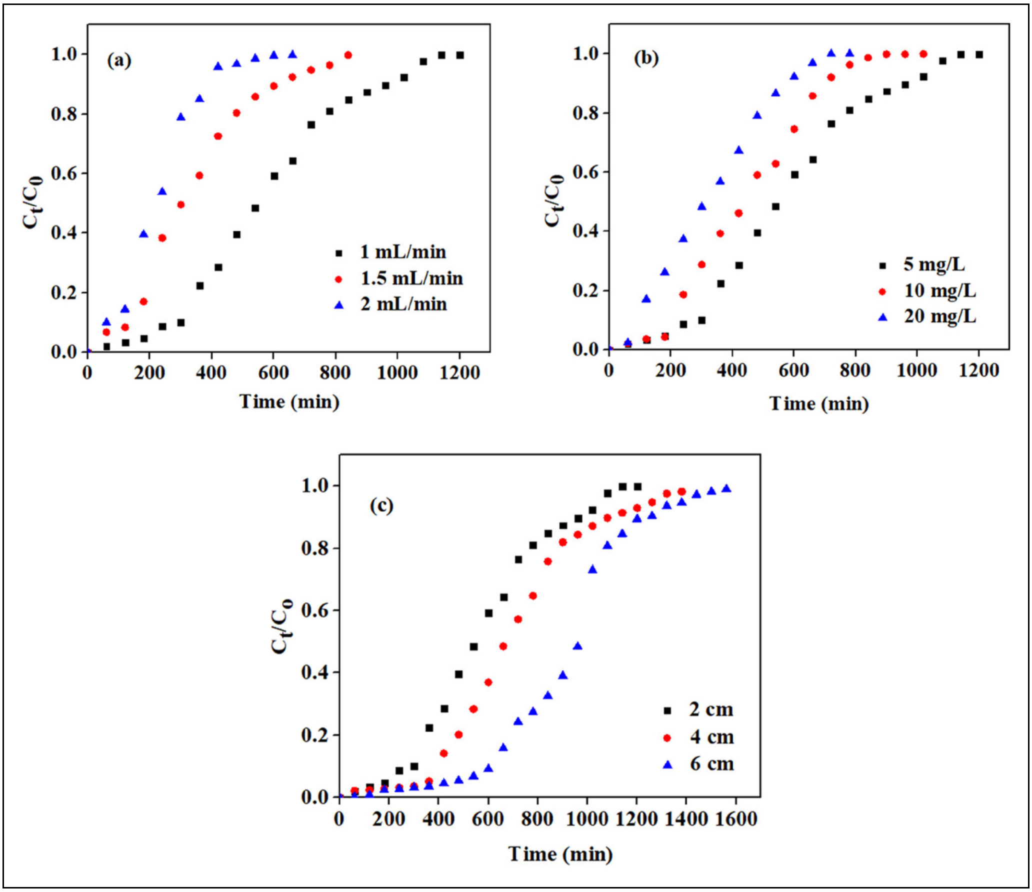

Figure 6. Experimental breakthrough curve of the fixed-bed column adsorption of F$^-$ onto the EKM adsorbent at different (a) flow rate (mL min^{-1}), (b) initial fluoride concentration (mg L^{-1}), and (c) bed depth (cm). EKM: MgO-impregnated eggshell–kaolin.

However, there was an increase in the equilibrium adsorption capacity (2.84, 4.42, and 6.48 mg g^{-1}) with the rise of initial fluoride concentration. This may be ascribed to the greater driving force provided by the high fluoride concentration to overcome the fixed-bed mass transfer resistance as described by previous studies (Chakraborty et al., 2021; Zhang et al., 2019). The values of the MTZ (1.47, 1.60, and 1.83 cm) also increased with increasing initial fluoride concentration.

Effect of bed depth. The effect of bed depth was studied by adjusting the column's bed depth to 2, 4, and 6 cm. The solution, with an initial fluoride concentration of 5 mg L^{-1}, was passed through the column at a flow rate of 1 mL min^{-1}, a temperature of 25 °C, and a pH of 7. The experimental results (Figure 6(c)) show that breakthrough times (300, 360, and 600 min) and exhaustion times (1140, 1380, and 1560 min) increased as bed depth increased. The equilibrium adsorption capacity (2.84, 3.49, and 4.57 mg g^{-1}), effluent volume (1140, 1380, and 1560 mL), and the MTZ (1.47, 2.96, and 3.69 cm) also rose with increased bed depth. This rise in equilibrium adsorption capacity likely results from longer residence time, allowing fluoride ions to diffuse deeper into the EKM adsorbent. Furthermore, increasing bed depth offers more

Table 2. Experimental parameters of the breakthrough curves from the adsorption of fluoride onto EKM adsorbent.

C_0 (mg L^{-1})	Bed depth (cm)	Flow rate (mL min^{-1})	t_b (min)	t_e (min)	V_{eff} (mL)	q_{tot} (mg)	q_e (mg g^{-1})	MTZ (cm)	EBCT (min)
5	2	1	300	1140	1140	2.84	2.84	1.47	1.69
10	2	1	180	900	900	4.42	4.42	1.60	1.69
20	2	1	60	720	720	6.48	6.48	1.83	1.69
5	2	1	300	1140	1140	2.84	2.84	1.47	1.69
5	2	1.5	180	840	840	2.51	2.51	1.57	1.13
5	2	2	120	660	660	1.14	1.14	1.64	0.85
5	2	1	300	1140	1140	2.84	2.84	1.47	1.69
5	4	1	360	1380	1380	3.49	3.49	2.96	3.39
5	6	1	600	1560	1560	4.57	4.57	3.69	5.09

EKM: MgO-impregnated eggshell–kaolin; MTZ: mass transfer zone; EBCT: empty bed contact time.

active sites for fluoride binding, which can delay both breakthrough and exhaustion times. A similar observation is documented by other researchers (Kumari et al., 2021; William et al., 2025).

Breakthrough curve modeling

Breakthrough curve modeling is essential for understanding and predicting the dynamic behavior of fixed-bed column adsorption systems (Kumari et al., 2021). Various mathematical breakthrough curve models have been applied to analyze and describe lab-scale column studies. In this study, three models: the Thomas, Clark, and Yoon–Nelson models, were employed at different flow rates, initial fluoride concentrations, and bed depths to evaluate the effects of these parameters on adsorption performance and to gain insights into the underlying mass transfer mechanisms (Kumari et al., 2021; William et al., 2025).

Thomas model. The Thomas model is one of the most frequently used models in fixed-bed column adsorption research. Its core assumptions include: (i) plug flow within the adsorption bed (no axial dispersion), (ii) adsorption–desorption processes follow pseudo-second-order reversible adsorption kinetics, (iii) equilibrium adheres to a Langmuir isotherm, and (iv) that external and intra-particle diffusion resistances are insignificant (Cruz et al., 2020; Geleta et al., 2021; Kumari et al., 2021). These simplifications make the Thomas model a valuable tool for predicting breakthrough behavior and estimating two primary parameters: the maximum adsorption capacity of the column bed ($q_{\max}$) and the rate constant (k_{th}). The linearized mathematical expression for the Thomas model is provided below:

$$\ln\left(\frac{C_0}{C_t} - 1\right) = \frac{K_{\text{th}} \times Q_{\text{th}} \times m}{Q} - K_{\text{th}} \times C_0 \times t \quad (9)$$

where C_0 (mg L^{-1}) and C_t (mg L^{-1}) represent the initial fluoride concentration and effluent fluoride concentration at a specific time t, the parameters K_{th} (L mg^{-1} min^{-1}), Q_{th} (mg g^{-1}), m (g), and Q (mL min^{-1}) represent the Thomas rate constant, adsorption capacity, mass of the adsorbent in the fixed-bed column, and flow rate, respectively. The plot of $\ln(C_0 / C_t - 1)$ against time (t) as shown in Figure 7 was used to estimate the values of K_{th} and Q_{th} from the slope and intercept, respectively.

The values of K_{th}, Q_{th}, and the correlation coefficient (R^2) for the Thomas model at varying flow rates, initial fluoride concentrations, and bed depths are provided in Table 3. The correlation coefficient ranged from 0.85 to 0.99, indicating that the Thomas model effectively describes the experimental breakthrough curve data obtained at different flow rates, initial fluoride concentrations, and bed depths. As the flow rate increased from 1 to 2 mL min^{-1}, the values of K_{th} increased due to the fast-moving solution, whereas the values of Q_{th} decreased. The decrease could be attributed to insufficient time of interaction between the fluoride ions in the fast-moving solution with the adsorbent in the fixed-bed column (Kumari et al., 2021). On the other hand, the values of Q_{th} increased with increasing initial fluoride concentration from 5 to 20 mg L^{-1}. This may be due to an increase in concentration gradient that acts as a driving force for the interaction of F^{-} ions with the adsorbent (Kumari et al., 2021). The Q_{th} values also increased with increasing bed depth. This has been linked to the existence of sufficient interactions between the F^{-} ions in the solution and more active sites provided by a deeper adsorbent bed (Chakraborty et al., 2021).

Clark model. The Clark model has been widely used in breakthrough modeling, as it integrates mass transfer kinetics with the Freundlich isotherm to describe the transport of adsorbate through a fixed-bed adsorbent. Its underlying assumptions include: (i) adsorption follows the Freundlich equilibrium, (ii) breakthrough behavior is governed by the rate of mass transfer in the bed, and (iii) the system approximates ideal plug flow without significant axial dispersion (Bakhta et al., 2024). The linearized expression for the Clark model is provided below:

$$\ln[(C_0 / C_t)^{n-1} - 1)] = -rt + \ln A \qquad (10)$$

where C_0 (mg L^{-1}) and C_t (mg L^{-1}) represent the initial influent fluoride concentration and effluent fluoride concentration at a specific time t, the parameters A and r (min^{-1}) denote the Clark model constants related to adsorption capacity and rate, respectively, and n is the Freundlich constant obtained from batch experiments ($n = 1.746$). The values of A and r (min^{-1}) were estimated from the intercept and slope of the plot (Figure 8).

From Table 3, the correlation coefficient (R^2) ranged from 0.84 to 0.99 for the Clark model, suggesting it can also describe the experimental data of the breakthrough curves. Increased flow rate has led to a decrease in A, which is in agreement with other works (Kumari et al., 2021; William et al., 2025). On the other hand, the increasing r values with increasing flow rate may be associated with the fast-moving fluoride solution to the adsorbent in the fixed bed. As the initial fluoride concentration rises from 5 to 20 mg L^{-1}, the constants A and r increase. This is consistent with previous studies (Kumari et al., 2021; William et al., 2025). Similarly, on increasing the bed depth, A increases, but r values decrease. This variation could be ascribed to a deeper adsorbent bed provides more active sites to bind the F^{-} ions in the solution (Kumari et al., 2021; William et al., 2025).

Yoon–Nelson model. Another model commonly used to predict breakthrough behavior in fixed-bed column adsorption is the Yoon–Nelson model. This model helps estimate the time needed for a 50% breakthrough (τ, min) and the rate constant (K_{YN}) that influences the steepness of the breakthrough curve. The linearized expression for the Yoon–Nelson model is displayed in equation (11), which is used to plot Figure 9:

$$\ln\left(\frac{C_t}{C_0 - C_t}\right) = K_{\mathrm{YN}} \times t - \tau K_{\mathrm{YN}} \qquad (11)$$

where C_0 (mg L^{-1}) and C_t (mg L^{-1}) represent the initial influent fluoride concentration and effluent fluoride concentration at a specific time t, the parameters K_{YN} (L min^{-1}) and τ (min) are the Yoon–Nelson constants. The R^2 values for the Yoon–Nelson model ranged from 0.85 to 0.99, also indicating its suitability in explaining the experimental data for the breakthrough curves. It is observed that, as the flow rate increased, the τ values decreased. This suggests that, at high flow rate, saturation of the bed is attained faster, resulting in less breakthrough time (William et al., 2025). The observation is also consistent with the results revealed in Figure 6(a). The increasing K_{YN} could be ascribed to insufficient time for F^{-} ions to interact with the adsorbent. The increase in initial fluoride concentration has also led to the rise in K_{YN} and decrease in τ, which can also be linked to the saturation of the active sites on the adsorbent with F^{-} ions. These results are similar

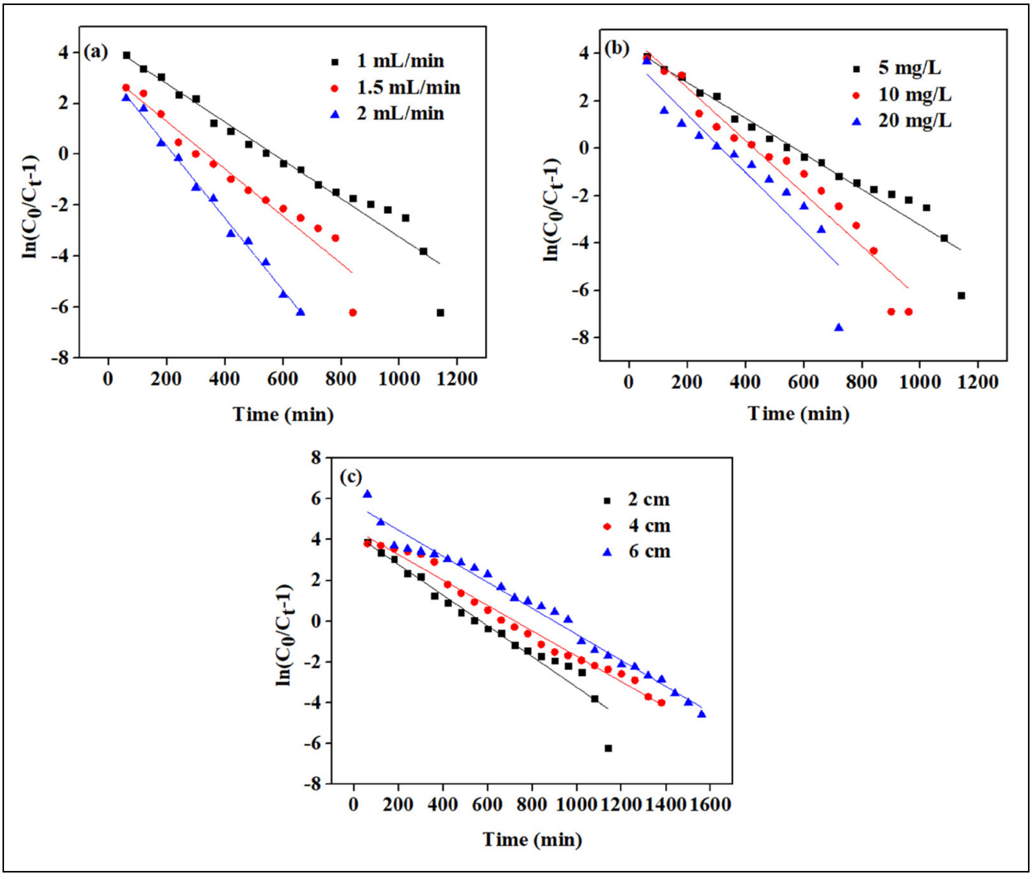

Figure 7. Thomas breakthrough curve modeling for fixed-bed column adsorption of F^- onto the EKM adsorbent at different (a) flow rates ($mL\,min^{-1}$), (b) initial F^- concentrations ($mg\,L^{-1}$), and (c) bed depths (cm). EKM: MgO-impregnated eggshell–kaolin.

to results observed by previous research (William et al., 2025). The increase in bed depth results in a reduction and enhancement of K_{YN} and τ values, respectively. This may be due to the increase in the adsorbent amount with increasing bed depth (Kumari et al., 2021).

Comparison of the Thomas, Clark, and Yoon–Nelson models. At lower influent concentrations (5–10 $mg\,L^{-1}$), all models provided good fits ($R^2 \geq 0.94$), with the Thomas model estimating adsorption capacities (q_{max}) of 2.84–6.35 $mg\,g^{-1}$. However, at 20 $mg\,L^{-1}$, the predictive performance declined ($R^2 = 0.85$), indicating that column non-idealities such as axial dispersion and intraparticle diffusion become more pronounced at higher loading. The Clark and Yoon–Nelson constants similarly reflected accelerated breakthrough at elevated concentrations, with a marked decrease in the 50% breakthrough time (τ) from 568.04 to 315.56 min. These results confirm that higher influent concentrations increase the driving force for adsorption but lead to earlier exhaustion of adsorption sites and reduced column efficiency. Flow rate exerted a strong influence on adsorption performance. Increasing flow rate from 1 to 2 $mL\,min^{-1}$ resulted in a decline in q_{max} (2.84–2.25 $mg\,g^{-1}$) and τ (568.04–223.39 min), attributable to

Table 3. Parameters of the Thomas, Clark, and Yoon–Nelson model for fixed-bed column adsorption of F^- onto EKM adsorbent at varied bed depth, initial fluoride concentration, and flow rate.

Thomas model				Clark model			Yoon–Nelson		
C_0 (mg L^{-1})	q_{max} (mg g^{-1})	K_{th} (L/mg min^{-1})	R^2	A	r (min^{-1})	R^2	K_{YN} (L min^{-1})	τ (min)	R^2
5	2.84	1.51×10^{-3}	0.95	30.73	0.007	0.94	0.008	568.04	0.95
10	6.35	7.53×10^{-4}	0.95	52.18	0.010	0.94	0.011	428.52	0.95
20	6.32	6.13×10^{-4}	0.85	23.82	0.012	0.84	0.012	315.56	0.85
Flow rate (mL min^{-1})									
1	2.84	1.51×10^{-3}	0.95	30.73	0.007	0.94	0.008	568.04	0.95
1.5	2.54	1.86×10^{-3}	0.94	12.19	0.009	0.93	0.009	338.46	0.94
2	2.25	2.82×10^{-3}	0.99	13.21	0.014	0.99	0.014	223.39	0.99
Bed depth (cm)									
2	2.84	1.51×10^{-3}	0.95	30.73	0.007	0.94	0.008	568.04	0.95
4	3.61	1.25×10^{-3}	0.98	35.22	0.006	0.99	0.006	686.57	0.98
6	4.49	1.28×10^{-3}	0.98	97.38	0.006	0.98	0.006	897.57	0.98

EKM: MgO-impregnated eggshell–kaolin.

shortened contact time between F^- ions and the adsorbent. Although the overall uptake capacity decreased, model fits improved substantially at higher flow rates ($R^2 \approx 0.99$), suggesting that kinetic-based models capture the rapid breakthrough behavior more effectively under dynamic conditions. Bed depth significantly enhanced the adsorption performance. As the bed depth increased from 2 to 6 cm, q_{max} rose from 2.84 to 4.49 mg g^{-1} and τ extended from 568.04 to 897.57 min, consistent with the BDST principle.

Generally, the Thomas, Yoon–Nelson, and Clark models applied in this study are based on the assumptions of ideal plug flow, negligible axial dispersion, minimal intra-particle diffusion resistance, and uniform bed porosity. The generally high coefficients of determination ($R^2 = 0.84$–0.99) and the systematic variation of model parameters with operating conditions support the applicability of these models under the present experimental conditions. Increases in the Thomas and Yoon–Nelson rate constants with flow rate, together with the corresponding decrease in τ, reflect reduced contact time and sharper breakthrough fronts, while increases in q_{max} and τ with bed depth are consistent with longer EBCT and extended MTZ lengths. The relatively stable EBCT values and well-defined MTZ behavior indicate uniform packing and stable hydrodynamic conditions, suggesting that non-ideal transport effects were not dominant. Nevertheless, future studies incorporating axial dispersion and intra-particle diffusion models would provide a more mechanistic understanding of fluoride transport, particularly at higher influent concentrations and flow rates.

BDST model. The BDST model is another widely used model for the continuous fixed-bed column adsorption studies. It has been modified from the Bohart–Adams equation (Sikha et al., 2025; Zhang et al., 2019). The BDST model predicts the time a column can operate effectively before saturation occurs, commonly referred to as the service time. In this study, the service time was determined in relation to the WHO guideline value of 1.5 mg L^{-1} fluoride, representing the threshold concentration (C_b, mg L^{-1}) beyond which the effluent is no longer considered safe for consumption.

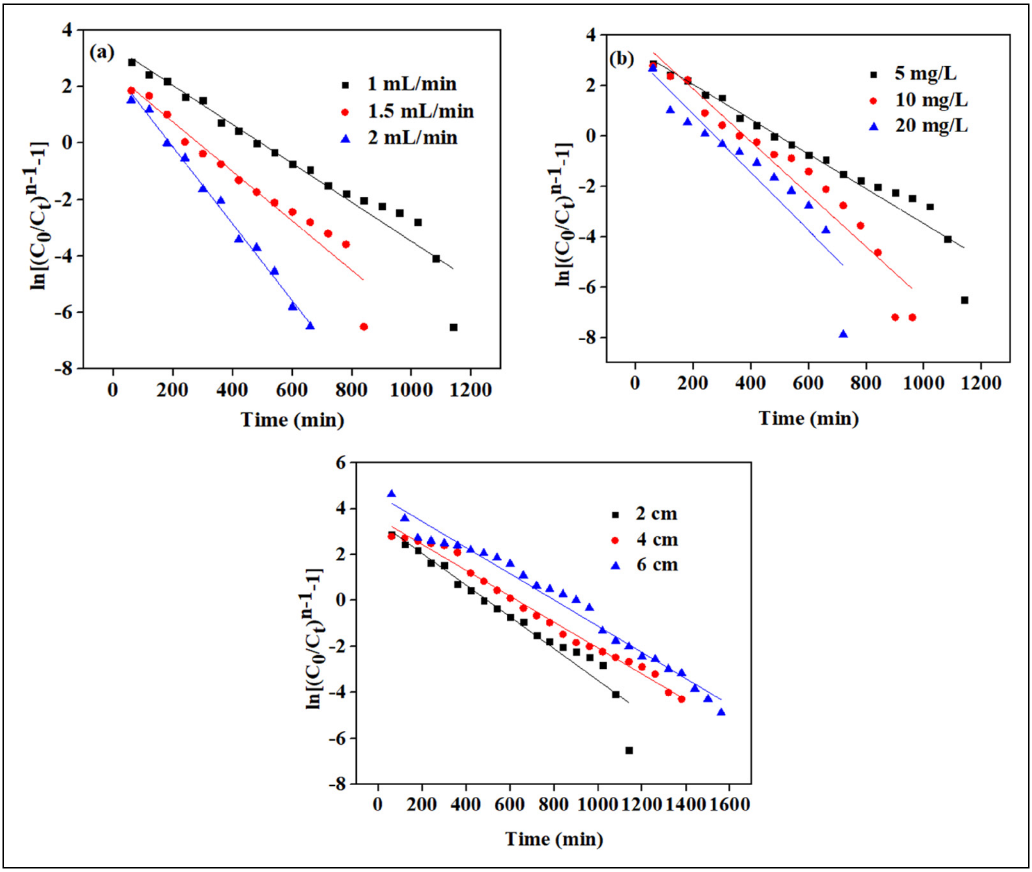

Figure 8. Clark breakthrough curve modeling for fixed-bed column adsorption of F^- onto EKM adsorbent at different (a) flow rates ($mL\,min^{-1}$), (b) initial F^- concentrations ($mg\,L^{-1}$), and (c) bed depths (cm). EKM: MgO-impregnated eggshell–kaolin.

The significance of the BDST model lies in its ability to relate bed depth to service time, thereby facilitating the estimation of how long a given adsorbent column can treat wastewater before replacement or regeneration is required. The linearized mathematical expression for the BDST model, as proposed by Hutchins, is given below (Hutchins, 1973):

$$t = \frac{N_0 Z}{C_0 u} - \frac{1}{K_\alpha C_0} \ln\left(\frac{C_0}{C_b} - 1\right) \qquad (12)$$

where K_α ($L\,mg^{-1}\,min^{-1}$), N_0 ($mg\,L^{-1}$), u ($cm\,min^{-1}$), t (min), Z (cm), C_0 ($mg\,L^{-1}$), and C_b ($mg\,L^{-1}$) represent the BDST rate constant, saturation concentration, linear velocity, service time, bed depth, influent and effluent fluoride concentrations at breakthrough, respectively.

The plot of t (min) against Z (cm) is displayed in Figure 10. From the figure, the service time is observed to increase with increasing bed depth. This may be attributed to the increase in the amount of adsorbent, which increases its adsorption capacity (Kumari et al., 2021; Zhang et al., 2019). The values of K_α and N_0 were obtained from the intercept and slope, respectively. The values of K_α and N_0 determined were 4.33×10^{-3} ($L\,mg^{-1}\,min^{-1}$) and 436.11 ($mg\,L^{-1}$). The correlation coefficient ($R^2 \geq 0.97$) of the linear fitting suggests that the BDST model

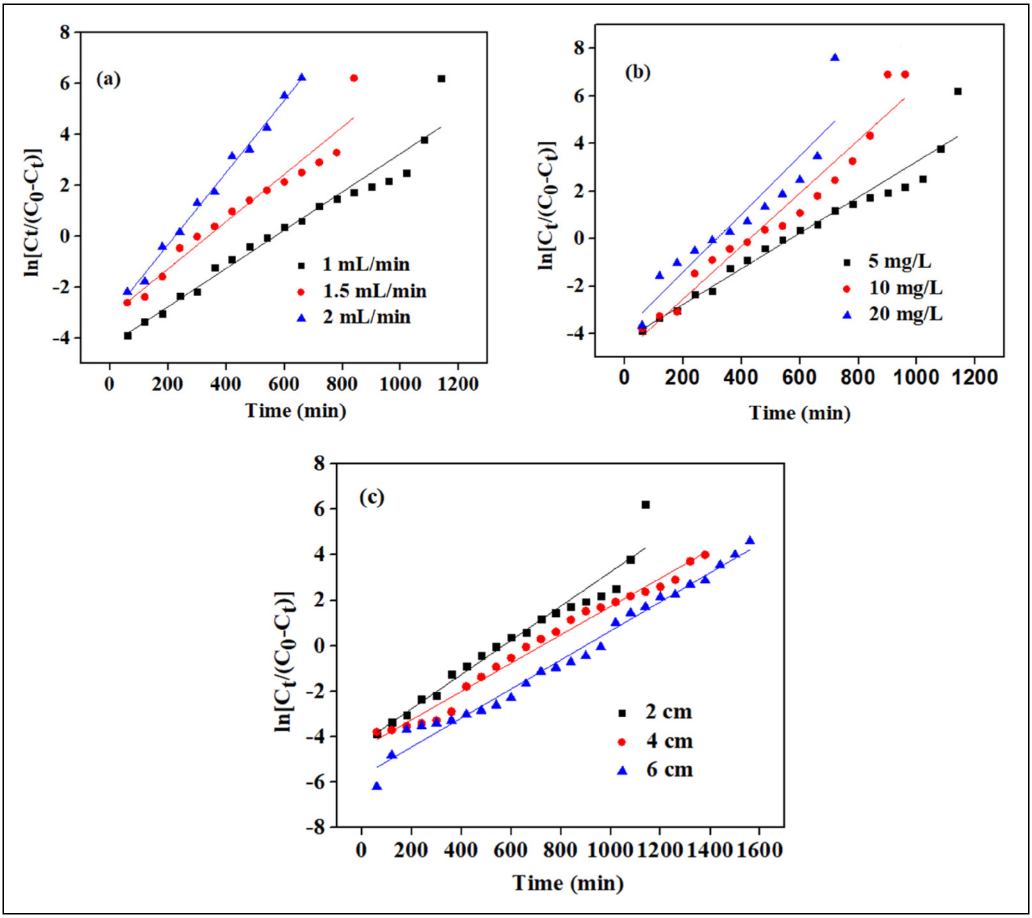

Figure 9. Yoon–Nelson breakthrough curve modeling for fixed-bed column adsorption of F^- onto EKM adsorbent at different (a) flow rates ($mL\,min^{-1}$), (b) initial F^- concentrations ($mg\,L^{-1}$), and (c) bed depths (cm).

explains the experimental data well. It was observed that the time required for the column to reduce fluoride concentration to the safe limit of 1.5 $mg\,L^{-1}$ was 480, 360, and 180 min for bed depths of 6, 4, and 2 cm, respectively. Correspondingly, the volumes of effluent treated at these bed depths were 480, 360, and 180 mL.

Reusability study

Regeneration of the adsorbent was performed to evaluate its reusability over three consecutive cycles. After each adsorption process, the column was rinsed with 0.1 M NaOH solution at a flow rate of 1 $mL\,min^{-1}$ to desorb the fluoride ions. This was followed by washing with deionized water until a neutral pH was reached. The regenerated adsorbent was then reused for three adsorption cycles, and the effluent fluoride concentration was recorded to evaluate the adsorbent's stability and regeneration performance. Figure 11 shows the changes in the breakthrough curves when the fixed-bed column is reused for the four cycles. The consecutive increase of the reusability cycle has led to a left shift and shorter

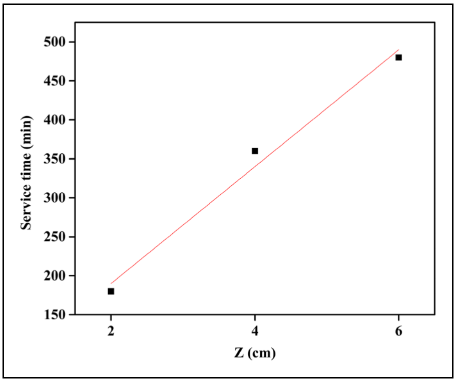

Figure 10. Bed depth service time model for fixed-bed column adsorption of F^- onto EKM adsorbent ($Q = 1$ mL min^{-1}, $C_0 = 10$ mg L^{-1} at pH 7). EKM: MgO-impregnated eggshell–kaolin.

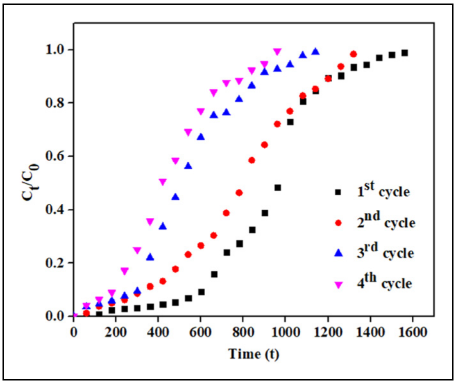

Figure 11. Reusability study of EKM on fixed-bed column adsorption. EKM: MgO-impregnated eggshell–kaolin.

breakthrough times with minimal breakthrough and exhaustion times. The breakthrough times for the first, second, third, and fourth cycles were 600, 420, 300, and 180 min, respectively, while the corresponding exhaustion times were 1560, 1320, 1140, and 960 min, indicating a progressive decrease in column performance with repeated use. This behavior may be attributed to the gradual saturation of the active sites, resulting from irreversible fluoride binding at surface Mg- and Ca-based sites, partial loss or transformation of Mg- and Ca-based active sites during alkaline NaOH regeneration, and accumulation of Mg–F and Ca–F surface complexes within mesopores, which increases diffusion resistance. Additionally, repeated regeneration and washing cycles may cause particle rearrangement and bed compaction, further contributing to earlier breakthrough with successive reuse cycles (Kumari et al., 2021).

Effect of co-existing anions

The assessment of competing anions such as phosphate (PO_4^{3-}), nitrate (NO_3^-), sulfate (SO_4^{2-}), and chloride (Cl^-) is critical in fluoride adsorption studies, as the presence of co-existing ions in natural waters can significantly affect the adsorption performance (de Carvalho Costa et al., 2024). In this study, the influence of individual anions on fluoride adsorption by the EKM adsorbent was evaluated by introducing 50 mg L^{-1} solutions of PO_4^{3-}, NO_3^-, SO_4^{2-}, and Cl^- separately, while maintaining an initial fluoride concentration of 5 mg L^{-1}.

The influence of co-existing anions on fluoride adsorption was evident from both the breakthrough behavior (Figure 12(a)) and the total adsorption capacities (Figure 12(b)). Among the anions, the breakthrough curve of PO_4^{3-} was the shortest, followed by SO_4^{2-}, while NO_3^- showed a moderate breakthrough time and Cl^- exhibited the longest curve. The breakthrough and exhaustion times further illustrate this trend: for the blank column, $t_b = 600$ min and $t_e = 1560$ min, whereas in the presence of PO_4^{3-}, these values decreased markedly to 300 and 900 min, respectively. SO_4^{2-} also shortened the run to $t_b = 300$ min and $t_e = 1020$ min, while NO_3^- resulted in intermediate times of 420 and 1260 min. Cl^- displayed delayed breakthrough and exhaustion time (540 and 1380 min), indicating its relatively weaker competition compared to the other anions. These breakthrough results are consistent with the equilibrium adsorption capacities, which decreased from 4.567 mg g^{-1} in the blank to 4.294 mg g^{-1} (−6.0%) with Cl^-, 3.898 mg g^{-1} (−14.6%) with NO_3^-, 2.998 mg g^{-1} (−34.3%) with SO_4^{2-},

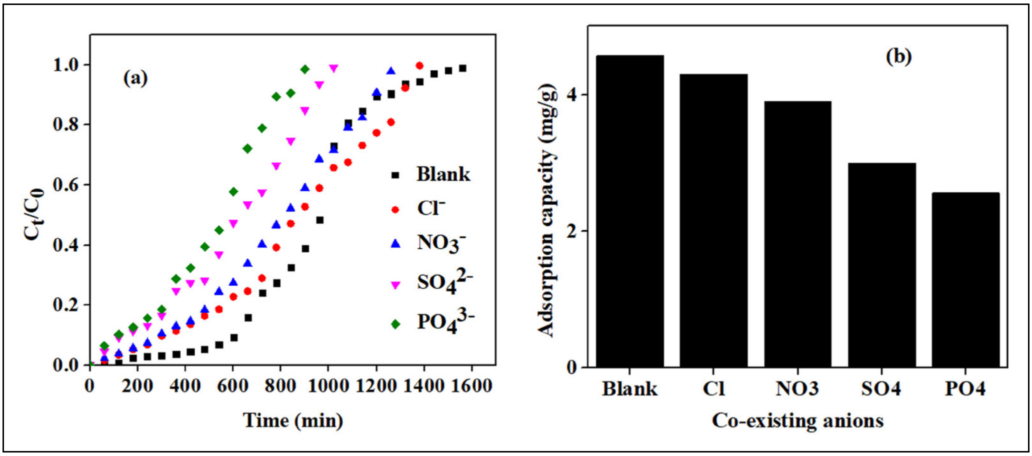

Figure 12. Effect of co-existing anions on (a) breakthrough curves, and (b) adsorption capacity for the fixed-bed column adsorption of F^- onto EKM adsorbent. EKM: MgO-impregnated eggshell–kaolin.

Table 4. Comparison of EKM composite with other adsorbents for fluoride removal in a fixed-bed column system.

Adsorbent	Initial F^- conc.	Bed depth (cm)	Flow rate (mL min^{-1})	Adsorption capacity (mg g^{-1})	Reference
Bone char	10	13	5	6.28	Nigri et al. (2020)
Volcanic rocks	10	10	1.25	0.11	Geleta et al. (2021)
$CaCO_3$	5	-	0.43	0.011	Wong and Stenstrom (2018)
Alumina	40	7.5	1.5	19.12	Kumari et al. (2021)
$Al(OH)_3$/HAp composite	10	10	15	1.28	William et al. (2025)
Al–Mg–Ca-coated sand	5	-	2	0.183	Modaresahmadi et al. (2025)
Zirconium oxide-coated scoria	10	10	1.25	0.058	Geleta et al. (2022)
Marble waste-derived hydroxyapatite	10	25	16.7	1.21	Mehta et al. (2024)
Bentonite clay	5	10	15	2.88	Kalsido et al. (2021)
Eggshell/kaolin/MgO	10	2	1	6.35	Present study

EKM: MgO-impregnated eggshell–kaolin.

and 2.558 mg g^{-1} (−44.0%) with PO_4^{3-}. The observed order of inhibitory effect, $PO_4^{3-} > SO_4^{2-} > NO_3^- > Cl^-$, agrees with previous reports that multi-valent oxyanions, particularly phosphate and sulfate, strongly suppress fluoride uptake through inner-sphere complexation and competition for active hydroxylated sites, while mono-valent ions such as chloride and nitrate exert weaker effects (Nabbou et al., 2019; Ravulapalli and Ravindhranath, 2019). This trend can be explained by differences in ionic radius, charge density, and the resulting binding affinity of the competing anions toward the active sites of the EKM adsorbent. Trivalent phosphate (PO_4^{3-}), which possesses a high charge and relatively small effective ionic radius, exhibits the highest charge density and charge to radius (Z/r) ratio, leading to strong electrostatic attraction and inner-sphere complex formation with surface active sites. Consequently, PO_4^{3-} shows the strongest competitive effect against fluoride adsorption. In contrast, divalent sulfate (SO_4^{2-}) and mono-valent nitrate (NO_3^-) and chloride (Cl^-), which have lower charge densities and larger hydrated ionic radii, interact more weakly with the adsorbent surface, resulting in minimal competition with fluoride ions.

Cost analysis

From this study, it was observed that water with safe fluoride levels of 1.5 mg L^{-1} can be obtained at ~180 min, during which 0.18 L of water is treated using 1 g of the EKM adsorbent. Extrapolating from this performance, only 11.11 g of adsorbent would be required to produce 2 L of defluoridated water, which corresponds to the average daily water intake per person. This relatively small quantity of material demonstrates the efficiency of the composite in producing safe drinking water with minimal adsorbent usage.

The raw materials required for composite preparation are inexpensive and locally accessible. Eggshells are an abundant waste byproduct with negligible acquisition cost. Kaolin, sourced from Tanzania, has an indicative cost of approximately USD0.04 per kg, while magnesium nitrate hexahydrate [$Mg(NO_3)_2 \cdot 6H_2O$], the precursor for MgO, is available at about USD3–5 per kg. Based on these values, the cost of producing 11.11 g of adsorbent, sufficient to treat 2 L of drinking water, would be only a fraction of USD1. Furthermore, the potential to regenerate and reuse the adsorbent over multiple cycles would further reduce the material demand and cost per liter of safe water produced, thereby enhancing its sustainability. These results highlight the potential of the EKM composite as an affordable and sustainable defluoridation material for use in fluoride-affected regions.

Comparison with other adsorbents

The adsorption capacity of the EKM adsorbent used in this study for the uptake of F^- ions from the solution on a fixed-bed column setting was compared with other adsorbents. The adsorption capacities reported for different adsorbents differ depending on the experimental conditions, such as bed depth, initial fluoride concentration, and influent flow rate, as presented in Table 4. The results obtained in this study have demonstrated that the EKM adsorbent recorded a high adsorption capacity similar to that reported in previous studies.

Conclusion

The study demonstrated that the synthesized EKM composite is an efficient, low-cost, and sustainable adsorbent for fluoride removal from water using a fixed-bed column system. The composite exhibited a mesoporous structure with a large surface area of 158.5 $m^2\,g^{-1}$, enhancing ion exchange and surface adsorption. The column performance was strongly influenced by operational parameters. Increasing the flow rate reduced the breakthrough time from 300 to 120 min and the exhaustion time from 1140 to 660 min due to shorter contact periods, while increasing the initial fluoride concentration raised the adsorption capacity from 2.84 to 6.48 mg g^{-1} but shortened the breakthrough time from 300 to 60 min. Increasing the bed depth extended breakthrough and exhaustion times from 300 to 600 min and from 1140 to 1560 min, respectively, owing to the availability of more active sites. The Thomas, Clark, and Yoon–Nelson models provided excellent fits ($R^2 \geq 0.94$), and the BDST model predicted a service time of 480 min at a 6 cm bed depth before effluent fluoride reached 1.5 mg L^{-1}. Co-existing anions influenced adsorption performance, with inhibitory effects following the order: $PO_4^{3-} > SO_4^{2-} > NO_3^- > Cl^-$. The

EKM composite maintained good reusability over four cycles, confirming its high efficiency, economic viability, and potential for practical defluoridation in fluoride-affected regions. Future studies combining batch adsorption experiments with zeta potential analysis and pH-dependent uptake tests are recommended to determine the primary adsorption mechanism.

Acknowledgments

The authors would like to acknowledge the Nelson Mandela African Institution of Science and Technology and the University of Dodoma for their help and support in carrying out this research work successfully.

ORCID iDs

Aisha Murgen Kitemangu https://orcid.org/0000-0002-3169-7643
Revocatus Lazaro Machunda https://orcid.org/0000-0003-4308-3910
Mwemezi Johaiven Rwiza https://orcid.org/0000-0001-5526-444X
Nyemaga Masanje Malima https://orcid.org/0000-0002-0753-1475
Andrew Toyi Banyikwa https://orcid.org/0000-0002-9769-4699
Gordian Rocky Mataba https://orcid.org/0000-0003-1288-802X

Funding

The authors received no financial support for the research, authorship, and/or publication of this article.

Declaration of conflicting interests

The authors declared no potential conflicts of interest with respect to the research, authorship, and/or publication of this article.

Data availability

All the data used to support the findings of this study are included in the article.

References

Alhassan SI, Huang L, He Y, et al. (2021) Fluoride removal from water using alumina and aluminum-based composites: A comprehensive review of progress. *Critical Reviews in Environmental Science and Technology* 51: 2051–2085.

Assami Z and Messaitfa A (2023) Use of eggshell as a low-cost alternative adsorbent for elimination of fluoride from groundwater. *Pollution* 9: 39–55.

Ayalew AA (2020) Development of kaolin clay as a cost-effective technology for defluoridation of groundwater. *International Journal of Chemical Engineering* 2020: 8820727.

Ayodeji AA, Modupe OE, Rasheed B, et al. (2018) Data on CaO and eggshell catalysts used for biodiesel production. *Data in Brief* 19: 1466–1473.

Bakhta S, Sadaoui Z, Bouazizi N, et al. (2024) Successful removal of fluoride from aqueous environment using $Al(OH)_3$@AC: Column studies and breakthrough curve modeling. *RSC Advances* 14: 1–14.

Borgohain X, Boruah A, Sarma GK, et al. (2020) Rapid and extremely high adsorption performance of porous MgO nanostructures for fluoride removal from water. *Journal of Molecular Liquids* 305: 112799.

Chakraborty A and Naskar MK (2021) Study on the synthesis and structural properties of zeolite A–MgO composite for defluoridation of water. *Transactions of the Indian Ceramic Society* 80: 199–207.

Chakraborty M, Pandey M and Pandey P (2021) Fixed bed column performance of *Tinospora cordifolia* for defluoridation of water. *Water Supply* 21: 2324–2332.

Chaudhary M, Jain N and Maiti A (2021) A comparative adsorption kinetic modeling of fluoride adsorption by nanoparticles and its polymeric nanocomposite. *Journal of Environmental Chemical Engineering* 9: 105595.

Chen N, Zhang Z, Feng C, et al. (2010) Fluoride removal from water by granular ceramic adsorption. *Journal of Colloid and Interface Science* 348: 579–584.

Cruz MAP, Guimarães LCM, da Costa Júnior EF, et al. (2020) Adsorption of crystal violet from aqueous solution in continuous flow system using bone char. *Chemical Engineering Communications* 207: 372–381.

Das L, Das P, Bhowal A, et al. (2021) Enhanced biosorption of fluoride by extracted nanocellulose/ polyvinyl alcohol composite in batch and fixed-bed system: ANN analysis and numerical modeling. *Environmental Science and Pollution Research* 28: 47107–47125.

de Carvalho Costa LR, Jurado-Davila IV, Oliveira JTD, et al. (2024) Exploring key parameters in adsorption for effective fluoride removal: A comprehensive review and engineering implications. *Applied Sciences* 14: 2161.

Deju R, Mazilu C, Stanculescu I, et al. (2020) Fourier transform infrared spectroscopic characterization of thermal treated kaolin. *Romanian Reports in Physics* 72: 806.

Fadaei A (2021) Comparison of water defluoridation using different techniques. *International Journal of Chemical Engineering* 2021: 2023895.

Feng J, Wang Z, Zhang W, et al. (2021) Insight into the ion exchange in the adsorptive removal of fluoride by doped polypyrrole from water. *Environmental Science and Pollution Research* 28: 67267–67279.

Geleta WS, Alemayehu E and Lennartz B (2021) Volcanic rock materials for defluoridation of water in fixed-bed column systems. *Molecules* 26: 77.

Geleta WS, Alemayehu E and Lennartz B (2022) Fixed-bed adsorption: Comparisons of virgin and zirconium oxide-coated scoria for the removal of fluoride from water. *Molecules* 27: 2527.

He Q, Luo Y, Feng Y, et al. (2020) Biochar produced from tobacco stalks, eggshells, and mg for phosphate adsorption from a wide range of pH aqueous solutions. *Materials Research Express* 7: 115603.

Hutchins RA (1973) New method simplifies design of activated carbon systems. *Chemical Engineering* 80: 133–138.

Ijumulana J, Ligate F, Irunde R, et al. (2021) Spatial uncertainties in fluoride levels and health risks in endemic fluorotic regions of Northern Tanzania. *Groundwater for Sustainable Development* 14: 100618.

Kalsido AW, Kumar A, Tekola B, et al. (2021) Evaluation of bentonite clay in modified and unmodified forms to remove fluoride from water. *Water Science and Technology* 84: 2661–2674.

Kimambo V, Bhattacharya P, Mtalo F, et al. (2019) Fluoride occurrence in groundwater systems at global scale and status of defluoridation—State of the art. *Groundwater for Sustainable Development* 9: 100223.

Kumari U, Mishra A, Siddiqi H, et al. (2021) Effective defluoridation of industrial wastewater by using acid modified alumina in fixed-bed adsorption column: Experimental and breakthrough curves analysis. *Journal of Cleaner Production* 279: 123645.

Lee J-I, Hong S-H, Lee C-G, et al. (2021) Fluoride removal by thermally treated egg shells with high adsorption capacity, low cost, and easy acquisition. *Environmental Science and Pollution Research* 28: 35887–35901.

Lin C, Liu B, Pu L, et al. (2021) Photocatalytic oxidation removal of fluoride ion in wastewater by g-C_3N_4/TiO_2 under simulated visible light. *Advanced Composites and Hybrid Materials* 4: 339–349.

Liu B, Ai L, Lei M, et al. (2023) Efficient fluoride removal using nano MgO: Synthesis, mechanisms, and performance evaluation.

Mehta D, Saharan VK and George S (2024) Marble waste derived hydroxyapatite: Low-cost adsorbent for the defluoridation of drinking water. *Materials Today: Proceedings* 102: 175–185.

Modaresahmadi K, Khodadoust AP and Wescott J (2025) Defluoridation of water using Al–Mg–Ca ternary metal oxide-coated sand in adsorption column study. *Separations* 12: 19.

Nabbou N, Belhachemi M, Boumelik M, et al. (2019) Removal of fluoride from groundwater using natural clay (kaolinite): Optimization of adsorption conditions. *Comptes Rendus Chimie* 22: 105–112.

Nigri EM, Santos AL, Bhatnagar A, et al. (2020) Chemical regeneration of bone char associated with a continuous system for defluoridation of water. *Brazilian Journal of Chemical Engineering* 36: 1631–1643.

Okafor CO, Ude UI, Okoh FN, et al. (2024) Safe drinking water: The need and challenges in developing countries. In: Dincer S, Aysun Mercimek Takci H and Sumengen Ozdenefe M (eds) *Water Quality—New Perspectives*. IntechOpen.

Owusu-Agyeman I, Reinwald M, Jeihanipour A, et al. (2019) Removal of fluoride and natural organic matter from natural tropical brackish waters by nanofiltration/reverse osmosis with varying water chemistry. *Chemosphere* 217: 47–58.

Prathibha C, Biswas A, Chunduri LA, et al. (2020) Zr(IV) functionalized graphene oxide anchored sand as potential and economic adsorbent for fluoride removal from water. *Diamond and Related Materials* 109: 108081.

Rathnayake A, Hettithanthri O, Sandanayake S, et al. (2022) Essence of hydroxyapatite in defluoridation of drinking water: A review. *Environmental Pollution* 311: 119882.

Ravulapalli S and Ravindhranath K (2019) Novel adsorbents possessing cumulative sorption nature evoked from Al_2O_3 nanoflakes, *C. urens* seeds active carbon and calcium alginate beads for defluoridation studies. *Journal of the Taiwan Institute of Chemical Engineers* 101: 50–63.

Senarathna G, Wanniarachchi D and Diyabalanage S (2024) Fluoride removal in water using kaolin and eggshell powder blend adsorbents. *Universal Journal of Green Chemistry* 2: 275–292.

Setiadji S, Sundari C, Munir M, et al. (2018) Synthesis of solid catalyst from egg shell waste and clay for biodiesel production. *Journal of Physics: Conference Series* 1013: 012199.

Sikha S, Singh SB and Mandal B (2025) Investigating the efficacy of bimetallic metal–organic frameworks (MOFs) as fluoride adsorbent in fixed-bed adsorption columns: Experimental and modeling insights. *Journal of Water Process Engineering* 71: 107376.

Solanki YS, Agarwal M, Maheshwari K, et al. (2021) Removal of fluoride from water by using a coagulant (inorganic polymeric coagulant). *Environmental Science and Pollution Research* 28: 3897–3905.

Suwattanamala A, Bandis N, Tedsree K, et al. (2017) Synthesis, characterization and adsorption properties of Fe_3O_4/MWCNT magnetic nanocomposites. *Materials Today: Proceedings* 4: 6567–6575.

Tang X, Zhou C, Xia W, et al. (2022) Recent advances in metal–organic framework-based materials for removal of fluoride in water: Performance, mechanism, and potential practical application. *Chemical Engineering Journal* 446: 137299.

Tortajada C (2020) Contributions of recycled wastewater to clean water and sanitation Sustainable Development Goals. *NPJ Clean Water* 3: 22.

Wan K, Huang L, Yan J, et al. (2021) Removal of fluoride from industrial wastewater by using different adsorbents: A review. *Science of the Total Environment* 773: 145535.

Wang D-C, Xu M-D, Jin Z, et al. (2023) Synthesis and characterization of porous MgO nanosheet-modified activated carbon fiber felt for fluoride adsorption. *Nanomaterials* 13: 1082.

Wang X, Cheng H, Chai P, et al. (2020) Pore characterization of different clay minerals and its impact on methane adsorption capacity. *Energy & Fuels* 34: 12204–12214.

Wang X, Li N, Li J, et al. (2019) Fluoride removal from secondary effluent of the graphite industry using electrodialysis: Optimization with response surface methodology. *Frontiers of Environmental Science & Engineering* 13: 1–11.

Wang Z, Su J, Ali A, et al. (2021) Microbially induced calcium precipitation based simultaneous removal of fluoride, nitrate, and calcium by *Pseudomonas* sp. WZ39: Mechanisms and nucleation pathways. *Journal of Hazardous Materials* 416: 125914.

William O, Meshesha BT, Mussa M, et al. (2025) Highly efficient $Al(OH)_3$/HAp composite adsorbent for the removal of fluoride from drinking water: Batch and column studies. *Applied Water Science* 15: 88.

Wong EY and Stenstrom MK (2018) Onsite defluoridation system for drinking water treatment using calcium carbonate. *Journal of Environmental Management* 216: 270–274.

Workeneh K, Zereffa EA, Segne TA, et al. (2019) Eggshell-derived nanohydroxyapatite adsorbent for defluoridation of drinking water from Bofo of Ethiopia. *Journal of Nanomaterials* 2019: 2458312.

Zhang Y, Xiong L, Xiu Y, et al. (2019) Defluoridation in fixed bed column filled with Zr(IV)-loaded garlic peel. *Microchemical Journal* 145: 476–485.